

Experimental characterization of two-particle entanglement through position and momentum correlations

Andrea Bergschneider^{1,2,3}, Vincent M. Klinkhamer^{1,3}, Jan Hendrik Becher¹, Ralf Klemt¹, Lukas Palm¹, Gerhard Zürn¹, Selim Jochim¹ and Philipp M. Preiss^{1*}

Quantum simulation is a rapidly advancing tool for gaining insight into complex quantum states and their dynamics. Trapped-ion systems have pioneered deterministic state preparation and comprehensive state characterization, operating on localized and thus distinguishable particles¹. With ultracold atom experiments, one can prepare large samples of delocalized particles, but the same level of characterization has not yet been achieved². Here, we present a method to measure the positions and momenta of individual particles to obtain correlations and coherences. We demonstrate this with deterministically prepared samples of two interacting ultracold fermions in a coupled double well³. As a first application, we use our technique to certify and quantify different types of entanglement^{4–6}.

Ultracold atoms in optical lattice systems can be probed through site-resolved imaging⁷. This procedure gives access to correlations on the level of individual particles and directly reveals charge and spin order in lattice systems². Many important aspects of the available quantum states, however, are not accessible by position-space imaging alone: properties such as long-range coherence, currents and phase fluctuations are related to off-diagonal order, or coherences, in the many-body states. Time-of-flight imaging of quantum gases in momentum space can in principle probe such coherences⁸, but has only been possible for systems of many particles, often leading to inhomogeneous averaging. A central goal for ultracold-atom experiments is the development of new methods that access real-space order as well as coherences (Fig. 1a).

In this Letter we show that single-particle resolved measurements of atomic momenta can reveal the coherence properties of small systems^{6,9}. We demonstrate this for a Fermi–Hubbard double well^{3,10}, for which we measure two-body correlations in position and momentum space (Fig. 1b). This approach enables us to tightly constrain the full density matrix of the two-particle system in different regimes of attractive, repulsive or vanishing interaction.

The key motivation for such a characterization is to describe a state through its entanglement properties¹¹. The presence of entanglement certifies the non-separability of a state with respect to a particular partitioning of the Hilbert space and constitutes the most prominent difference between classical and quantum mechanics^{12,13}. The characterization of entanglement can be useful for applications in quantum metrology¹⁴, for example.

In lattice systems of ultracold atoms, different types of entangled states may occur: for states with exactly one particle per site, entanglement between internal degrees of freedom of localized particles

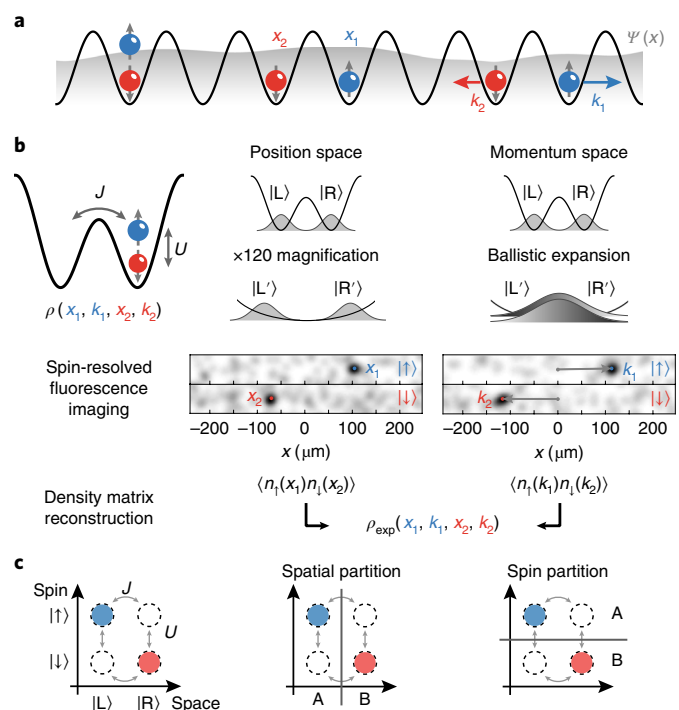


Fig. 1 | Detection of many-body systems in conjugate bases. a, A quantum system is defined by its many-body wavefunction $\Psi(x)$ (grey). A system with number fluctuations can be characterized naturally with correlation functions in the positions x_i or the momenta k_i of its constituent particles. **b**, We measure single-particle spin-resolved correlations in position and momentum space for a two-site Fermi–Hubbard system, which we use to infer information about the density matrix ρ of the initial state. **c**, The spinful Hubbard dimer forms a four-mode system. Different types of quantum correlation, or entanglement, can emerge between subsystems defined by spatial or spin partitions (A and B).

can be described by spin models similar to trapped-ion or superconducting-qubit systems. Such states can be created in optical lattices¹⁵ or through deterministic or probabilistic schemes in optical tweezers^{16,17}. Conceptually more challenging situations occur for indistinguishable, mobile particles: in such cases, particles are not

¹Physikalisches Institut der Universität Heidelberg, Heidelberg, Germany. ²Present address: Institute for Quantum Electronics, ETH Zurich, Zurich, Switzerland. ³These authors contributed equally: Andrea Bergschneider, Vincent M. Klinkhamer. *e-mail: preiss@physi.uni-heidelberg.de

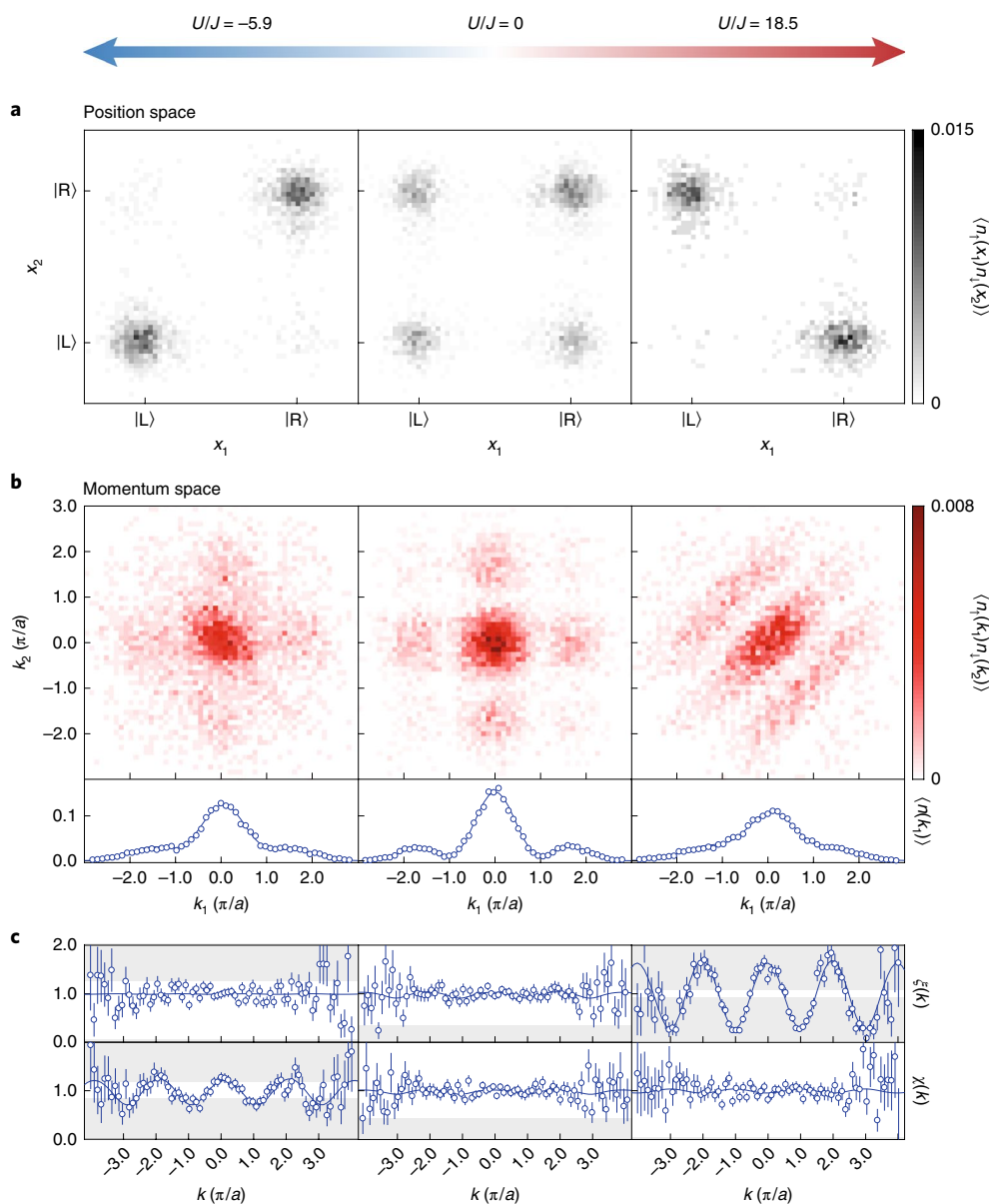


Fig. 2 | Correlations in the Hubbard dimer. **a**, The spin-resolved spatial correlation function $\langle n_i(\alpha)n_j(\beta) \rangle$ exhibits mostly double occupancies for attractive interactions (left), no correlations in the non-interacting case (centre) and strong suppression of double occupancies for repulsive interactions (right). **b**, For non-interacting particles, the momentum-space correlation function $\langle n_i(k_1)n_j(k_2) \rangle$ (top row) is separable and shows an interference pattern in the single-particle coordinates. The single-particle coherence is visible as side peaks in the single-particle momentum density $\langle n_i(k_i) \rangle \equiv \langle n_i(k_1) \rangle + \langle n_i(k_2) \rangle$ (bottom row). For strong attractive (repulsive) interactions, single-particle coherence is suppressed, but interference patterns emerge along the diagonal (antidiagonal), which signals the presence of two-particle coherence. **c**, Integrated momentum-difference and momentum-sum correlations, expressed as pair correlators $\chi(k)$ and $\xi(k)$, respectively. Entanglement can be certified if the data extend into the grey-shaded regions. Error bars represent the standard error of the mean and continuous lines are obtained from reconstructed momentum-space correlation functions (see Supplementary Information).

distinguishable by their spatial location and cannot be identified as the carriers of quantum correlations. It is then more appropriate to consider the mode entanglement between different spatial regions^{11,13}, as measured in recent experiments^{18,19}. How to fully describe entanglement in situations with fluctuating local particle number and symmetrization constraints enforced by quantum statistics has been the subject of intense debate in the literature^{4,5,20–23}.

The scenario that we consider here allows the study of various forms of entanglement in a single experiment (Fig. 1c): we populate two spatial modes with two particles that are distinguishable by their spin state³. From one point of view, entanglement between the particles is driven by interaction-induced correlations between their

motional states, which we identify experimentally. On the other hand, we can focus on the entanglement between the two spatial modes, which is largest in the non-interacting regime with maximal particle number fluctuation. We verify and quantify entanglement, both between the spin modes and the spatial modes, through measurements of the Rényi entropy^{13,19}, and characterize its dependence on the interactions in the system.

The experimental system consists of two ⁶Li atoms confined to a double-well potential formed by optical tweezers with a waist of 1.15 μm and a wavelength of $\lambda = 1,064 \text{ nm}$ (ref. ³). The partially overlapping optical tweezers are tunnel-coupled with rate J , and on-site interactions U between atoms in hyperfine states

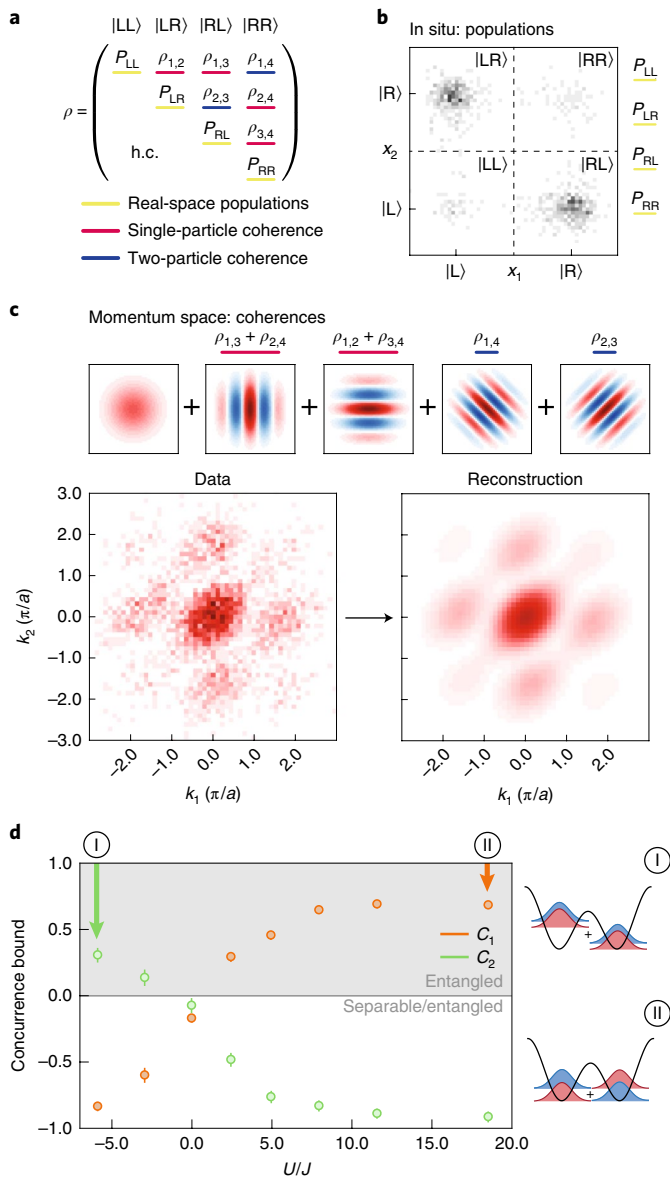


Fig. 3 | Evaluation of the concurrence from the measured correlation functions. **a**, The dimer density matrix ρ contains the full state information of real-space order as well as coherence properties. **b**, We obtain the in situ populations directly from the position-space correlation function. **c**, The magnitude and phase of the single- and two-particle coherences are encoded in the momentum-space correlation function as oscillations along the one- and two-particle coordinates. **d**, The lower bounds C_1 , C_2 of the concurrence certify entanglement (grey region) for all interacting systems studied in our experiments, with error bars corresponding to one standard deviation of statistical and systematic uncertainty (see Supplementary Information). The side panels visualize the changing character of the wavefunction, with its $|\uparrow\rangle$ and $|\downarrow\rangle$ components sketched in blue and red. For strong attractive and repulsive interactions, the ground state approaches two-body Bell states.

$|\uparrow\rangle = |F=1/2, m_F = +1/2\rangle$ and $|\downarrow\rangle = |F=3/2, m_F = -3/2\rangle$ are controlled via a magnetic Feshbach resonance. Together, this results in a Hubbard Hamiltonian

$$H = -J \sum_{\sigma} (\hat{c}_{L\sigma}^{\dagger} \hat{c}_{R\sigma} + \hat{c}_{R\sigma}^{\dagger} \hat{c}_{L\sigma}) + U \sum_{j=L,R} \hat{n}_{j\uparrow} \hat{n}_{j\downarrow} \quad (1)$$

with spatial modes L and R, where $\hat{c}_{i\sigma}^{(\dagger)}$ is the fermionic annihilation (creation) operator of a particle with spin σ on site i and $\hat{n}_{j\sigma} = \hat{c}_{j\sigma}^{\dagger} \hat{c}_{j\sigma}$. As demonstrated previously³, we initialize the system with one particle per spin state near its ground state by adiabatically transferring two deterministically prepared particles from a single optical tweezer to a dual-tweezer configuration. We then adiabatically tune the tunnelling rate J and the on-site interaction U via the depth of the optical tweezers and the magnetic field, respectively.

We now demonstrate how to obtain the position-space order and coherences of the experimentally initialized state. Our method is similar to recent proposals^{6,9} and in close analogy to two-photon experiments working with near- and far-field correlations²⁴: We combine atom-resolved measurements of correlations in position and momentum space, which we obtain through a novel, spin-resolved free-space detection method²⁵.

To access particle correlations in momentum space, we release the atoms from the tweezers into a large, elongated optical dipole trap. This allows expansion along the axis connecting the double well, while confining the atoms in the perpendicular directions (see Methods and ref. 25). After a ballistic expansion for one-quarter trap period, the quantum state corresponds to the Fourier transform of the initial state. By using resonant single-atom imaging and separate exposures for the two spin states within each experimental realization (cf. ref. 25), we record the particle momenta k_1 and k_2 (Fig. 1b). After several thousand iterations of the experiment, we can reconstruct the momentum correlation function $\langle n_1(k_1)n_1(k_2) \rangle$.

To probe the spatial correlations we measure the occupation of each site in a spin-resolved manner. We make use of a position-mapping method, where we first project the quantum state on the single-site occupation basis by quickly decoupling the wells and then impart a site-specific momentum. This separates the spatial modes after time-of-flight for direct spatially resolved imaging (see Methods). We thus obtain the in situ density distribution and determine spin-resolved correlation functions $\langle n_i(\alpha)n_i(\beta) \rangle$ (Fig. 1b), where α, β denote the spatial modes {L,R}.

Figure 2 shows the measured spin-resolved correlation functions for the Fermi-Hubbard dimer near its ground state for different interaction strengths (see Supplementary Information). As theoretically expected, we directly observe that increasing repulsion (attraction) results in increasing anticorrelations (correlations) in position space (Fig. 2a). Simultaneously single-particle coherences disappear and a two-particle coherence appears, as is visible in momentum space (Fig. 2b). We analyse the data by extracting the pair correlators $\xi(d) = \frac{\int dk \langle n_1(k-d/2)n_1(k+d/2) \rangle}{\int dk \langle n_1(k-d/2) \rangle \langle n_1(k+d/2) \rangle}$ and $\chi(s) = \frac{\int dk \langle n_1(k+s/2)n_1(-k+s/2) \rangle}{\int dk \langle n_1(k+s/2) \rangle \langle n_1(-k+s/2) \rangle}$ in the relative and centre-of-mass

momentum coordinates $d=k_1-k_2$ and $s=k_1+k_2$, respectively, analogous to the noise correlation experiments performed in ref. 8 (Fig. 2c). For all measurements with interactions, the observed signal differs from 1, confirming the presence of pair correlations.

The observed correlations qualitatively agree with the expectations for the ground state in this highly controlled scenario. An essential question is how to use such experimental data to certify and quantify entanglement^{15-19,22}. Here, we are specifically interested in entanglement between particles, which we treat as distinguishable via their spin. Qualitatively, this question can be addressed by an entanglement witness (see Supplementary Information). The witness probes incompatibility with general product states (grey regions, Fig. 2c) and from our data certifies entanglement between particles for $|U/J| \gtrsim 5$.

A quantitative measure of the strength of entanglement between the particles is given by the concurrence²⁶. Although its exact determination requires knowledge of the full density matrix, we can construct lower bounds as $C_1 = 2(|\rho_{2,3}| - \sqrt{P_{LL}P_{RR}})$ and $C_2 = 2(|\rho_{1,4}| - \sqrt{P_{LR}P_{RL}})$ (refs. 16,23,27). Here, we have defined the

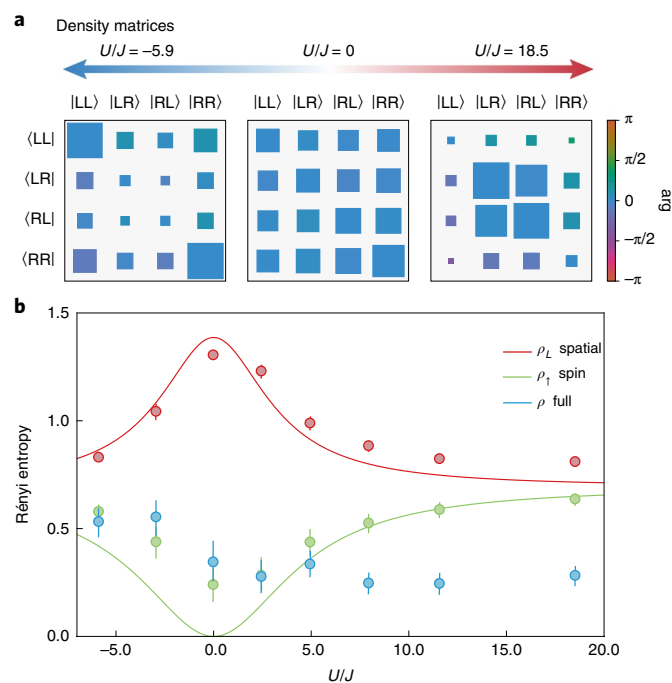


Fig. 4 | Entanglement entropy of the Hubbard dimer. **a**, To calculate entanglement entropy, we reconstruct the density matrix with a Bayesian quantum state estimation. The magnitude of the density matrix elements is proportional to the area of the squares, normalized to 0.5. The argument (arg) of complex-valued density matrix elements is encoded in the colour scale. **b**, Entanglement can occur between different subsystems, which may be taken to be the spatial or spin modes of the Hubbard dimer defined in Fig. 1c. Entanglement is present if the Rényi entropy of a subsystem exceeds the Rényi entropy of the full system. We observe entanglement of spatial modes for all interaction strengths and entanglement of spin modes at large interaction strengths. Error bars correspond to 90% credible intervals. The lines show the mode entropies of the ground state of the Hubbard dimer (see Supplementary Information).

density matrix in a position representation $|\alpha\beta\rangle$, where α and β denote the spatial modes {L,R} of the $|\uparrow\rangle$ and $|\downarrow\rangle$ particle (Fig. 3a). For C_1 and C_2 , we can extract the required quantities directly from the measured correlations⁶: $\rho_{ij} \equiv P_{\alpha\beta}$ correspond to the populations of the spatial modes (Fig. 3b), while $\rho_{1,4}$, $\rho_{2,3}$ are two-particle coherences that become apparent in the momentum correlations as oscillations along the relative and centre-of-mass coordinates (Fig. 3c). A positive value of either C_1 or C_2 results in a concurrence $C(\rho) \geq \max(0, C_1, C_2) > 0$, which demonstrates the presence of entanglement (Fig. 3d).

Besides the entanglement between particles as measured by the concurrence, we are also interested in spatial mode entanglement between tweezer sites. Therefore, we study the entropy of entanglement¹³, which compares the Rényi or von Neumann entropy of generic partitions of a system to the entropy of the full system. If subsystems individually have a higher entropy than the combined system, this proves the presence of entanglement between them²⁸. We partition our system in spatial modes and spin modes (Fig. 1c), which allows us to determine the role of either type of entanglement in the different interaction regimes.

We can evaluate the entanglement entropy of subsystems directly from our correlation measurements (see Supplementary Information). Determination of the entropy of the full system, however, requires knowledge of the full density matrix or collective measurements on multiple copies¹⁹. To evaluate those density matrix elements that are not fully constrained by our correlation

measurements (see, for example, the sums in Fig. 3c), we implement a Bayesian estimate of the density matrix²⁹ such that it remains positive-semidefinite (Fig. 4a and Methods). From this density matrix we obtain a tightly constrained posterior distribution of the Rényi entropy of the full system (blue circles, Fig. 4b). Comparing it to the entropy of the different subsystems, we see that the entanglement between spatial modes is largest for no interactions, while entanglement between spin modes (which we identify with the particles) grows with increasing interaction strength⁵.

This disparate behaviour of spatial and spin modes is an example of the inequivalence of entanglement between different degrees of freedom within the same state^{5,11,20}. The entanglement between spin modes is the relevant quantity if the quantum state were to be used for quantum information processing or communication, where each party has control over exactly one spin sector. On the other hand, the entanglement entropy of spatial regions reflects the cost of classically representing a quantum state with particle number fluctuations in real space. Our experiment realizes and probes the smallest non-trivial quantum systems in which these inequivalent notions of entanglement are both present.

These results show the potential of combined spin-resolved position and momentum correlation functions as a tool to characterize quantum states. The spin resolution and single-particle sensitivity of the detection method can be maintained for systems with larger particle number. It could be applied to continuum systems, for example to superfluid droplets, or to measure order parameters in fermionic superfluids with non-trivial orbital symmetries³⁰. Further applications extend to correlated few-body complexes such as individual, isolated Efimov trimers or fractional quantum Hall puddles, which could be mapped out completely in momentum space.

Online content

Any methods, additional references, Nature Research reporting summaries, source data, extended data, supplementary information, acknowledgements, peer review information; details of author contributions and competing interests; and statements of data and code availability are available at <https://doi.org/10.1038/s41567-019-0508-6>.

Received: 4 July 2018; Accepted: 15 March 2019;

Published online: 22 April 2019

References

- Blatt, R. & Roos, C. F. Quantum simulations with trapped ions. *Nat. Phys.* **8**, 277–284 (2012).
- Gross, C. & Bloch, I. Quantum simulations with ultracold atoms in optical lattices. *Science* **357**, 995–1001 (2017).
- Murmann, S. et al. Two fermions in a double well: exploring a fundamental building block of the Hubbard model. *Phys. Rev. Lett.* **114**, 080402 (2015).
- Ghirardi, G., Marinatto, L. & Weber, T. Entanglement and properties of composite quantum systems: a conceptual and mathematical analysis. *J. Stat. Phys.* **108**, 49–122 (2002).
- Dowling, M. R., Doherty, A. C. & Wiseman, H. M. Entanglement of indistinguishable particles in condensed-matter physics. *Phys. Rev. A* **73**, 052323 (2006).
- Bonneau, M., Munro, W. J., Nemoto, K. & Schmiedmayer, J. Characterizing twin-particle entanglement in double-well potentials. *Phys. Rev. A* **98**, 033608 (2018).
- Ott, H. Single atom detection in ultracold quantum gases: a review of current progress. *Rep. Prog. Phys.* **79**, 054401 (2016).
- Fölling, S. et al. Spatial quantum noise interferometry in expanding ultracold atom clouds. *Nature* **434**, 481–484 (2005).
- Yannouleas, C., Brandt, B. B. & Landman, U. Interference, spectral momentum correlations, entanglement and Bell inequality for a trapped interacting ultracold atomic dimer: analogies with biphoton interferometry. *Phys. Rev. A* **99**, 013616 (2019).
- Desbuquois, R. et al. Controlling the Floquet state population and observing micromotion in a periodically driven two-body quantum system. *Phys. Rev. A* **96**, 053602 (2017).
- Tichy, M. C., Mintert, F. & Buchleitner, A. Essential entanglement for atomic and molecular physics. *J. Phys. B* **44**, 192001 (2011).

12. Amico, L., Osterloh, A. & Vedral, V. Entanglement in many-body systems. *Rev. Mod. Phys.* **80**, 517 (2008).
13. Horodecki, R., Horodecki, P., Horodecki, M. & Horodecki, K. Quantum entanglement. *Rev. Mod. Phys.* **81**, 865 (2009).
14. Pezzè, L., Smerzi, A., Oberthaler, M. K., Schmied, R. & Treutlein, P. Quantum metrology with nonclassical states of atomic ensembles. *Rev. Mod. Phys.* **90**, 035005 (2018).
15. Dai, H.-N. et al. Generation and detection of atomic spin entanglement in optical lattices. *Nat. Phys.* **12**, 783–787 (2016).
16. Kaufman, A. M. et al. Entangling two transportable neutral atoms via local spin exchange. *Nature* **527**, 208–211 (2015).
17. Lester, B. J. et al. Measurement-based entanglement of noninteracting bosonic atoms. *Phys. Rev. Lett.* **120**, 193602 (2018).
18. Cramer, M. et al. Spatial entanglement of bosons in optical lattices. *Nat. Commun.* **4**, 2161 (2013).
19. Islam, R. et al. Measuring entanglement entropy in a quantum many-body system. *Nature* **528**, 77–83 (2015).
20. Zanardi, P. Quantum entanglement in fermionic lattices. *Phys. Rev. A* **65**, 042101 (2002).
21. Wiseman, H. M. & Vaccaro, J. A. Entanglement of indistinguishable particles shared between two parties. *Phys. Rev. Lett.* **91**, 097902 (2003).
22. Fukuhara, T. et al. Spatially resolved detection of a spin-entanglement wave in a Bose–Hubbard chain. *Phys. Rev. Lett.* **115**, 035302 (2015).
23. Mazza, L., Rossini, D., Fazio, R. & Endres, M. Detecting two-site spin-entanglement in many-body systems with local particle-number fluctuations. *New J. Phys.* **17**, 013015 (2015).
24. Taguchi, G. et al. Measurement and control of spatial qubits generated by passing photons through double slits. *Phys. Rev. A* **78**, 012307 (2008).
25. Bergschneider, A. et al. Spin-resolved single-atom imaging of ${}^6\text{Li}$ in free space. *Phys. Rev. A* **97**, 063613 (2018).
26. Wootters, W. K. Entanglement of formation of an arbitrary state of two qubits. *Phys. Rev. Lett.* **80**, 2245–2248 (1998).
27. Jafarpour, M. & Sabour, A. A useful strong lower bound on two-qubit concurrence. *Quantum Inf. Process.* **11**, 1389–1402 (2012).
28. Mintert, F. & Buchleitner, A. Observable entanglement measure for mixed quantum states. *Phys. Rev. Lett.* **98**, 140505 (2007).
29. Blume-Kohout, R. Optimal, reliable estimation of quantum states. *New J. Phys.* **12**, 043034 (2010).
30. Kitagawa, T., Aspect, A., Greiner, M. & Demler, E. Phase-sensitive measurements of order parameters for ultracold atoms through two-particle interferometry. *Phys. Rev. Lett.* **106**, 115302 (2011).

Acknowledgements

The authors acknowledge insightful discussions with A. Daley, N. Defenu, A. Elben, M. Gärtner, P. Hauke and M. Piani. This work has been supported by ERC consolidator grant 725636, DFG grant JO970/1-1, the Heidelberg Center for Quantum Dynamics and is part of the DFG Collaborative Research Centre SFB 1225 (ISOQUANT). A.B. acknowledges funding from the International Max-Planck Research School (IMPRS-QD). P.M.P. acknowledges funding from the European Union's Horizon 2020 programme under Marie Skłodowska-Curie grant agreement no. 706487 and from the Daimler and Benz Foundation.

Author contributions

A.B., V.M.K., G.Z., S.J. and P.M.P. conceived the experiment. A.B., V.M.K., J.H.B., R.K. and P.M.P. performed the experiment and, together with L.P., performed data analysis, developed theory and wrote the manuscript. All authors contributed to discussions about the experiment and manuscript. S.J. and P.M.P. supervised the project.

Competing interests

The authors declare no competing interests.

Additional information

Supplementary information is available for this paper at <https://doi.org/10.1038/s41567-019-0508-6>.

Reprints and permissions information is available at www.nature.com/reprints.

Correspondence and requests for materials should be addressed to P.M.P.

Journal peer review information: *Nature Physics* thanks Luca Pezzè and the other anonymous reviewer(s) for their contribution to the peer review of this work.

Publisher's note: Springer Nature remains neutral with regard to jurisdictional claims in published maps and institutional affiliations.

© The Author(s), under exclusive licence to Springer Nature Limited 2019

Methods

Experimental set-up. The double-well potential was realized by two overlapping optical tweezers with a waist of $1.15\ \mu\text{m}$ and a wavelength of $\lambda = 1,064\ \text{nm}$. We generated the two tweezers by applying two radio-frequency signals to an acousto-optical deflector, which allowed us to control the separation of the tweezers a as well as their relative and absolute depth. We prepared two ${}^6\text{Li}$ atoms near the ground state of the double well with a separation of $a = 1.5\ \mu\text{m}$ using the procedure described in ref. ³. We performed adiabatic ramps of the relative depth of the double well and then the magnetic offset field to increase the interaction strength. In this way, a Hubbard dimer was realized with tunnel coupling J controlled by the overall potential depth and with the interaction energy U tunable using a Feshbach resonance.

Single-atom imaging. We detected the individual atoms using a free-space single-atom, spin-resolved imaging technique²⁵ that provided a spatial resolution of $4\ \mu\text{m}$. The spin resolution was achieved by consecutive imaging pulses resonant on the individual transitions of the $|\uparrow\rangle$ and $|\downarrow\rangle$ hyperfine states and imaging of the fluorescence photons on different regions on the camera.

Momentum measurements. The momentum distribution was measured by combining the single-atom imaging with a time-of-flight expansion. After preparation, we switched off the double-well potential and let the quantum state expand in a weak optical potential that was elongated along the double-well axis with an aspect ratio of 8. After a quarter of the oscillation period along the elongated axis, we detected the position of the atoms and integrated over the directions perpendicular to the elongated axis of the potential. As the interactions are negligible during the expansion, the unitary evolution in the trap mapped the initial momentum distribution along the double-well axis to the position of the atoms along the elongated axis of the weak trap. The observed lattice momentum k_{lat} was in agreement with our expectation based on the double-well separation and the trap frequency during the time-of-flight. The data of the correlation function $\langle n_1(k_1)n_1(k_2) \rangle$ were obtained by averaging $\sim 4,000$ spin-resolved momentum measurements with a post-selection probability of $\geq 80\%$.

Position measurement. To resolve the in situ distribution of the atoms in the double-well potential, we projected the wavefunction onto the individual wells by diabatically increasing the trap depth of the double well. We then imprinted a diametrical centre-of-mass momentum onto the on-site wavefunctions of the two wells by a sudden change in the well separation to $3.2\ \mu\text{m}$ together with an expansion time of $6\ \mu\text{s}$. After that, we switched off the double well and performed a time-of-flight expansion before detecting the atoms. The parameters were optimized to obtain suitable magnification of the well separation as well as the on-site wavefunction. We obtained a fidelity for identifying each atom in the correct well of $99.4(3)\%$. The data for the spin-resolved spatial correlation function $\langle n_1(\alpha)n_1(\beta) \rangle$ were obtained from $\sim 1,000$ position measurements and a post-selection probability of $\geq 80\%$.

Evaluation of the density matrix elements. To determine the measured density matrix ρ_{exp} of a prepared state ρ of the Hubbard dimer, we read off the populations $P_{\alpha\beta}$ from the spatial correlation measurements. From the momentum correlation measurements we can extract the coherences. We calculated the momentum correlation function for ρ using the Fourier transforms of the single-particle basis states $\phi_\alpha = g(x \pm a/2) / \tilde{g}(k)e^{\mp iak/2}$, where $g(x)$ denotes the Wannier function and $\tilde{g}(k)$ is its Fourier transform. Neglecting the envelope function $\tilde{g}(k)$ in the following, we obtain the momentum-space correlation function

$$\begin{aligned} \langle n_1(k_1)n_1(k_2) \rangle = & 1 \\ & + 2\Re\{(\rho_{1,3} + \rho_{2,4})\} \cos ak_1 - 2\Im\{(\rho_{1,3} + \rho_{2,4})\} \sin ak_1 \\ & + 2\Re\{(\rho_{1,2} + \rho_{3,4})\} \cos ak_2 - 2\Im\{(\rho_{1,2} + \rho_{3,4})\} \sin ak_2 \\ & + 2\Re\{\rho_{2,3}\} \cos a(k_1 - k_2) - 2\Im\{\rho_{2,3}\} \sin a(k_1 - k_2) \\ & + 2\Re\{\rho_{1,4}\} \cos a(k_1 + k_2) - 2\Im\{\rho_{1,4}\} \sin a(k_1 + k_2) \end{aligned}$$

where the real and imaginary parts of the density matrix elements are explicitly written as coefficients of the trigonometric basis functions. This expression serves for creating basis functions (Supplementary Fig. 2) to obtain the off-diagonal matrix elements $\rho_{1,4}$, $\rho_{2,3}$ and so on. Note that we can only determine the sums $\rho_{1,3} + \rho_{2,4}$ and $\rho_{1,2} + \rho_{3,4}$ of the single-particle coherences with our measurement. For further details, see Supplementary Information.

Reconstruction of the density matrix. From the previously described method we obtained only a subset of the parameters required to unambiguously describe the density matrix of the prepared state. To avoid unphysical sets of density matrices and to estimate the effect of the statistical and systematic uncertainties from our data on the resulting density matrix entries, we reconstructed the density matrix ρ_{BME} using a Bayesian quantum state estimation as outlined in ref. ²⁹. All information about the experiment is contained in the likelihood function $\mathcal{L}(\rho) = p(\mathcal{M}|\rho)/p(\mathcal{M})$, a distribution over the measured data \mathcal{M} conditioned on a certain hypothesis about the state ρ , which quantifies the relative plausibility of the different possible states. The posterior distribution $\pi(\rho|\rho)$ was obtained by multiplying $\mathcal{L}(\rho)$ with a prior distribution $\pi_0(\rho)d\rho$ on the states. We chose the Hilbert–Schmidt prior as uninformative prior over all physical density matrices. The Bayesian mean estimate $\hat{\rho}_{\text{BME}}$ is then given by the mean of the posterior distribution. The expectation value of an observable \mathcal{O} can be calculated as $\langle \mathcal{O} \rangle = \int \mathcal{O}(\rho)\pi(\rho)d\rho$ with the errors given in terms of the credible interval of its posterior distribution. With the Bayesian estimate of the density matrix, we can evaluate the expected value of the Rényi entropy $S = -\log\text{Tr}(\rho^2)$ for the entire system and for different subsystems.

Data availability

The data that support the plots within this paper and other findings of this study are available from the corresponding author on reasonable request.